

Coherent control of the photoelectron angular distribution in ionization of neon by a circularly polarized bichromatic field in the resonance region

E. V. Gryzlova¹, M. M. Popova², A. N. Grum-Grzhimailo¹, E. I. Staroselskaya^{1,2}, N. Douguet^{3,4} and K. Bartschat⁵

¹*Skobeltsyn Institute of Nuclear Physics, Lomonosov Moscow State University, Moscow 119991, Russia*

²*Faculty of Physics, Lomonosov Moscow State University, Moscow 119991, Russia*

³*Department of Physics, University of Central Florida, Orlando, Florida 32816, USA*

⁴*Department of Physics, Kennesaw State University, Marietta, Georgia, 30060, USA*

⁵*Department of Physics and Astronomy, Drake University, Des Moines, Iowa 50311, USA*



(Received 6 July 2019; published 12 December 2019)

Coherent control of the photoelectron angular distribution (PAD) in ionization by a bichromatic circularly polarized field is theoretically studied in neon in the photon energy range 16–20 eV. The breakdown of the PAD axial symmetry with respect to the light propagation direction is analyzed. The coherent control of the PAD manifests itself through: (1) a change from a one-lobe to a three-lobe shape, respectively, for co- and counter-rotating harmonics, (2) a variation of the polar asymmetry with the light frequency, and (3) a rotation of the PAD around the direction of the beam depending on the relative phase between the harmonics. Tuning the lowest harmonic at the $2p^53s$ or $2p^54s$ intermediate excited states strongly influences the PAD. In contrast to atomic hydrogen and the alkali atoms, the cases of equal and opposite helicity are not related in neon. Features of a conjugate polarization setup, when one harmonic is linearly polarized while the other one is circularly polarized, are also discussed.

DOI: [10.1103/PhysRevA.100.063417](https://doi.org/10.1103/PhysRevA.100.063417)

I. INTRODUCTION

Quantum coherent control is ubiquitous in atomic, molecular, and solid-state physics, providing a fundamental basis for numerous methods to investigate quantum systems. The phase control of photoprocesses has been the subject of many studies and reviews [1–7]. Quantum coherent-control approaches have been applied to control chemical reactions or biological change [8], to ultrafast and nonlinear optics [9,10], 4D ultrafast electron microscopy [11,12], and other promising applications.

The implementation of highly coherent sources of extreme ultraviolet (XUV) radiation, such as seeded free-electron lasers (FELs), has made it possible to extend light-driven coherent control into the high-energy domain [13]. Coherent control of the photoelectron angular distributions (PADs) was recently achieved at FERMI [13] by manipulating the time delay (corresponding to the relative phase) between a linearly polarized fundamental field and its second harmonic to unprecedented accuracy. An asymmetry of the PAD was obtained by interfering one- and two-photon ionization pathways. An intermediate resonant state was employed as a stepping stone to enhance the two-photon ionization amplitude, thereby resulting in an increased interference signal.

Various aspects of coherent control of ionization in the XUV domain by association of the fundamental with either the second or third harmonic were discussed in [14], and its implementation to characterize unknown pulse parameters was successfully realized [15]. An extensive theoretical analysis of the control of the PAD after ionization by both linearly and circularly polarized bichromatic XUV radiation was

performed for ionization of the hydrogen atom in its ground state by tuning the fundamental harmonic near the intermediate $2p$ resonance [16,17]. In particular, the asymmetry of the PADs with respect to the plane normal to the electric field of the linearly polarized light, as well as the axial asymmetry of PADs with respect to the direction of the radiation beam for circularly polarized light, were studied, including their energy dependence near a resonant intermediate state. Further theoretical investigations were performed for bichromatic ionization of the valence $2p$ subshell of neon by linearly polarized light in the vicinity of the intermediate $2p^53s$ and $2p^54s$ states [18,19]. The latter analysis was conducted within lowest-order perturbation theory, for pulses with either finite or infinite durations, and also by solving the time-dependent Schrödinger equation (TDSE).

In the present work we develop a similar approach in neon for the case of circularly polarized co-propagating FEL harmonics and discuss other possible polarization setups. The present investigation was motivated by the fact that some linear and many nonlinear phenomena can manifest themselves in different ways, or possibly also disappear, depending on the light polarization, e.g., photoelectron spin polarization [20,21], stabilization [22,23], high-harmonic generation [24–27], or polarization-plane rotation [28]. Selection rules with circular radiation often allow fewer ionization channels compared to using linearly polarized light, thereby enhancing specific effects and simplifying their interpretation. A detailed description of multiphoton ionization with elliptically polarized light can, for instance, be found in Ref. [29]. Investigations of ionization processes with radiation of different polarizations provide detailed information on the ionization

amplitudes and may enable so-called “complete” (“perfect”) experiments [30] to be performed, as well as characterize the unknown parameters of the radiation [31,32].

There are two occurrences when a multicolor field appears: A short pulse with broad envelope and laser radiation with multiple harmonics. Both cases have been discussed extensively in the low-frequency domain, for both the multiphoton [33,34] and tunneling ionization [35] regimes. The asymmetry in the photoelectron emission was used to determine the carrier envelope phase (CEP) of few-cycle laser pulses [31] and to produce directional bond breaking in molecular ionization [36]. At high frequencies, multiphoton ionization can often be described in terms of lowest-order perturbation theory [37]. CEP effects and electron vortices in photoionization by an elliptically polarized ultrashort pulse were discussed for *s*-shell ionization [38,39]. Ionization by a fundamental ω and second harmonic 2ω has attracted much attention. It is, however, usually limited to the study of alkali atoms and molecules, due to the difficulty in manipulating the light polarization in the vacuum ultraviolet (VUV) domain. The $\omega + 2\omega$ scheme has been successfully achieved with linearly polarized radiation [40,41], but it could only be applied with circularly polarized radiation in a few limited cases [42]. For systems without spherical symmetry, such as molecules or atoms in external fields [43,44], interference between one- and two-photon ionization pathways appears in intricate ways. Recently, such interference was discussed for the case of chiral molecules [45], where circularly polarized beams are particularly important, as they enable discriminating different enantiomers and resolving their dynamics.

In this study we consider the coherent control of the PAD in ionization of neon by a coherent mixture of a circularly polarized fundamental pulse, with frequency ω , and its second harmonic 2ω in the photon energy range $\hbar\omega = 16\text{--}20$ eV, i.e., tuned near the $2p^5 3s$, $4s$, $3d$ discrete resonances (see Fig. 1, where an example of a transition scheme is given in the

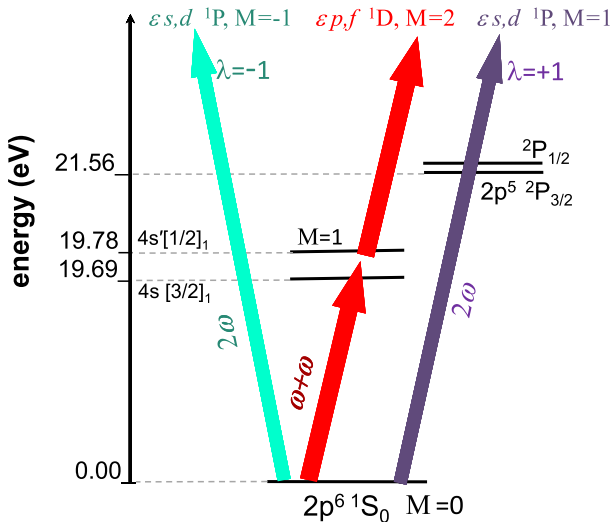


FIG. 1. Transition scheme for valence ionization of neon ground state by bichromatic radiation with a right-hand circularly polarized fundamental and a right-hand or left-hand circularly polarized second harmonic.

vicinity of the $4s$ states). The ionization of the $2p$ shell brings novel features to the process in comparison with ionization from the $1s$ ground state of atomic hydrogen [17].

In the next section we present our theoretical approach, which is followed by our results in Sec. III. In Sec. IV we discuss other practical polarization setups, and the final section is devoted to our conclusions. Unless stated otherwise, atomic units are used throughout this paper.

II. THEORY

The electric field for a right-hand circularly polarized fundamental (ω), and right-hand (positive helicity, $\lambda = +1$) or left (negative helicity, $\lambda = -1$) circularly polarized second harmonic (2ω) is of the form

$$\mathcal{E}(t) = F(t)\{\mathbf{x} \cos \omega t + \mathbf{y} \sin \omega t + \eta[\mathbf{x} \cos(2\omega t + \phi) + \lambda \mathbf{y} \sin(2\omega t + \phi)]\}. \quad (1)$$

The convention of helicities is in accordance with [46]. We take the pulse envelope in the form $F(t) = F_0 \sin^2[2\pi Nt/\omega]$, where N is the number of optical cycles, $\eta > 0$ is the ratio of the electric field strengths between the fundamental and the second harmonic, ϕ is the relative phase of the harmonics, and the z axis is chosen parallel to the radiation beams \mathbf{k}_γ . The peak intensity of the pulse is given as $I_\omega = 7 \times 10^{16} F_0^2$ W/cm², where F_0 is taken in atomic units.

We denote the amplitude for photoemission in the direction $\mathbf{k}/k \equiv \{\vartheta, \varphi\}$ by the second harmonic in first-order perturbation theory as $U^{(1)}(\mathbf{k})$, and the one by the fundamental in second order as $U^{(2)}(\mathbf{k})$, respectively. According to Fermi’s golden rule, the probability to observe an electron with energy $k^2/2 = 2\omega - \text{I.P.}$ (where I.P. is the ionization potential) is proportional to $|\eta U^{(1)}(\mathbf{k}) + U^{(2)}(\mathbf{k})|^2$. In evaluating the photoionization amplitudes $U^{(1)}(\mathbf{k})$ and $U^{(2)}(\mathbf{k})$ we follow the formalism of [19] for linearly polarized fields and obtain the photoelectron angular distribution as a sum of three terms:

$$\frac{dW}{d\Omega} = \frac{dW^{(I)}}{d\Omega} + \frac{dW^{(II)}}{d\Omega} + \frac{dW^{(III)}}{d\Omega}. \quad (2)$$

In the above equation, the first and second terms are due to the second harmonic (one-photon ionization) and the first harmonic (two-photon ionization), respectively, while the third term is due to interference between the two paths. The three terms can be cast into the forms

$$\frac{dW^I}{d\Omega} = \frac{\eta^2}{4\pi} \sum_k B_k^I P_k(\cos \vartheta), \quad (3)$$

$$\frac{dW^{II}}{d\Omega} = \frac{1}{4\pi} \sum_k B_k^{II} P_k(\cos \vartheta), \quad (4)$$

$$\frac{dW^{III}}{d\Omega} = \frac{\eta}{\sqrt{\pi}} \sum_k \hat{k}^{-1} \text{Re}[B_{kq}^{III} Y_{kq}(\vartheta, \varphi)]. \quad (5)$$

While both B^I and B^{II} are real, B^{III} is complex valued. There is no sum over q in Eq. (5) because, as will be shown below, choosing fixed polarizations of the harmonics allows only one value of q .

After performing the necessary algebra, we obtain

$$B_k^I = (-1)^{L_f+1} \sum_{l'l'} \hat{l} \hat{l}' (1\lambda, 1 - \lambda | k0) (l0, l'0 | k0) \begin{Bmatrix} 1 & 1 & k \\ l' & l & L_f \end{Bmatrix} \exp [i(\Delta_l^{(1)} - \Delta_{l'}^{(1)})] |T_\lambda^{(1)}|^2 D_{0 \rightarrow L_f l, 1}^{(0)} D_{0 \rightarrow L_f l', 1}^{(0)*}, \quad (6)$$

$$B_k^{II} = 5(-1)^{L_f} \sum_{\substack{l'l' \\ LL'S}} (-1)^{S+L+L'} \hat{L} \hat{L}' \hat{l} \hat{l}' (l0, l'0 | k0) (22, 2 - 2 | k0) \begin{Bmatrix} L & L' & k \\ l' & l & L_f \end{Bmatrix} \begin{Bmatrix} L & L' & k \\ 2 & 2 & S \end{Bmatrix} \\ \times \exp [i(\Delta_l^{(2)} - \Delta_{l'}^{(2)})] \left(\sum_{nL_n} \alpha_{10}^{\zeta_n*} \alpha_{L_n S}^{\zeta_n} T_{E_n}^{(2)} \begin{Bmatrix} S & L & 2 \\ 1 & 1 & L_n \end{Bmatrix} D_{0 \rightarrow n, 1}^{(0)} D_{n, L_n \rightarrow L_f l, L}^{(S)} \right) \\ \times \left(\sum_{n'L_n'} \alpha_{10}^{\zeta_{n'}*} \alpha_{L_n' S}^{\zeta_{n'}} T_{E_{n'}}^{(2)*} \begin{Bmatrix} S & L' & 2 \\ 1 & 1 & L_n' \end{Bmatrix} D_{0 \rightarrow n', 1}^{(0)*} D_{n', L_n' \rightarrow L_f l', L'}^{(S)*} \right), \quad (7)$$

$$B_{kq}^{III} = \frac{(-1)^{L_f}}{\sqrt{3}} \sum_{l'l'} \hat{l} \hat{l}' (l0, l'0 | k0) (1\lambda, 2 - 2 | kq) \begin{Bmatrix} 2 & 1 & k \\ l & l' & L_f \end{Bmatrix} \\ \times \exp [i(\Delta_l^{(1)} - \Delta_{l'}^{(2)})] T_\lambda^{(1)} D_{0 \rightarrow L_f l, 1}^{(0)} \left(\sum_{n'L_n'} |\alpha_{10}^{\zeta_{n'}}|^2 T_{E_{n'}}^{(2)*} D_{0 \rightarrow n', 1}^{(0)*} D_{n', L_n' \rightarrow L_f l', 2}^{(0)*} \right). \quad (8)$$

Here l is the orbital angular momentum of the photoelectron, standard notations for the Clebsch-Gordan coefficients, $6j$ symbols, Legendre polynomial, and spherical harmonic are used, and we defined $\hat{a} \equiv \sqrt{2a+1}$. In Eqs. (6)–(8) ζ_n and ζ_f (below) describe collectively any additional quantum numbers that may be needed to further identify a given state. The approximations and notations in Eqs. (6)–(8) are similar to those used previously to derive Eqs. (10)–(13) of [19]. Consequently, we only describe the main ideas below.

We assume a closed-shell atom in the initial state $|0\rangle$ and the LSJ -coupling scheme for the final ionic states with orbital angular momentum L_f , spin $S_f = \frac{1}{2}$, and total electronic angular momentum J_f . The result implies an incoherent summation over the fine-structure states J_f . The intermediate states in the second-order amplitude are described in the intermediate-coupling scheme. For the n th state we have

$$|\zeta_n J_n\rangle = \sum_{L_n S_n} \alpha_{L_n S_n}^{\zeta_n} |\zeta_n L_n S_n J_n\rangle. \quad (9)$$

We neglect the spin-orbit interaction in the atomic continuum, which is a very good approximation for a relatively light target such as neon. We then introduce the following short-hand notations for the reduced matrix elements $D^{(S)}$ of the dipole operator [47]:

$$D_{0 \rightarrow L_f l, 1}^{(0)} = \langle \zeta_f L_f l, L = 1 || D || 0 \rangle, \\ D_{n, L_n \rightarrow L_f l, L}^{(S)} = \langle \zeta_f L_f l : L || D^S || \zeta_n L_n \rangle, \\ D_{0 \rightarrow n, 1}^{(0)} = \langle \zeta_n L_n = 1 || D^{S_n=0} || 0 \rangle, \quad (10)$$

where the superscript (S) or (0) indicates the value of the conserved total spin. The electric dipole operator cannot change the spin of a system. For channels starting from the ground state, therefore, only $S = 0$ is allowed. For channels passing through the intermediate state, S could be either “0” and “1.” In Eqs. (6)–(8) $\alpha_{10}^{\zeta_n} \equiv \alpha_{L_n=1, S_n=0}^{\zeta_n}$. We also abbreviated $-ii^{-l} e^{i\delta_l} \equiv e^{i\Delta_l^{(1)}}$ and $-i^{-l} e^{i\delta_l} \equiv e^{i\Delta_l^{(2)}}$, where δ_l is the

scattering phase in the photoionization channel with orbital angular momentum l .

The time-dependent factors $T^{(1)}$ and $T_{E_n}^{(2)}$ were described in detail in [16, 17]. They are given by

$$T_{\lambda=\pm 1}^{(1)} = \mp e^{-i\phi} \frac{F_0}{\sqrt{2}} \int_0^{NT} \sin^2 \Omega t' e^{i(E-E_0-2\omega)t'} dt', \quad (11) \\ T_{E_n}^{(2)} = \frac{F_0^2}{2} \int_0^{NT} \sin^2 \Omega t' e^{i(E-E_n-\omega)t'} dt' \\ \times \int_0^{t'} \sin^2 \Omega t'' e^{i(E_n-E_0-\omega)t''} dt''. \quad (12)$$

Here the rotating-wave approximation was applied, and thus there are no fast-oscillating terms like $e^{i(E-E_0+2\omega)t}$. The relative phase ϕ , which is an important control parameter, can be decoupled as

$$T^{(1)} T_{E_n}^{(2)*} \sim e^{-i\phi}. \quad (13)$$

The above consequent of the RWA was checked for hydrogen example and found to be very well fulfilled for $N \geq 40$ optical cycles (see Fig. 2(c) of [17]).

As in the case of linearly polarized harmonics [19], only terms with $S = 0$ contribute to the interference cross section (8). Therefore, in (8) we used $L' = J' = 2$ for the final orbital and total angular momenta in the two-photon ionization.

The PAD (2) may be conveniently parametrized as

$$\frac{dW^+}{d\Omega} = \frac{W_0}{4\pi} [1 + \beta_2^+ P_2(\cos \vartheta) + \beta_4^+ P_4(\cos \vartheta) \\ + \beta_1^+ \sin \vartheta \cos(\varphi - \psi_1) - \beta_3^+ \sin^3 \vartheta \cos(\varphi - \psi_3)] \quad (14)$$

for equal helicities (co-rotating fields, +) and

$$\frac{dW^-}{d\Omega} = \frac{W_0}{4\pi} [1 + \beta_2^- P_2(\cos \vartheta) + \beta_4^- P_4(\cos \vartheta) \\ + \beta_3^- \sin^3 \vartheta \cos(3\varphi - \psi_3)] \quad (15)$$

for opposite helicities (counter-rotating fields, $-$). In both cases we assume the fundamental to be right-hand polarized. The situations when both harmonics are left-hand polarized or when the fundamental is left-hand and the second harmonic is right-hand polarized are related to (14) and (15), respectively, by the replacement $\varphi \rightarrow -\varphi$. The angular anisotropy parameters in (14) and (15) are

$$W_0 = \eta^2 B_0^I + B_0^{II}, \quad (16)$$

$$\beta_2^\pm = (\eta^2 B_2^I + B_2^{II})/W_0, \quad (17)$$

$$\beta_4^\pm = B_4^{II}/W_0, \quad (18)$$

$$\beta_1^+ = \eta |B_{1-1}^{III}/\sqrt{2} + B_{3-1}^{III}\sqrt{3}|/W_0, \quad (19)$$

$$\beta_3^+ = \eta 5\sqrt{3} |B_{3-1}^{III}|/(4W_0), \quad (20)$$

$$\beta_3^- = \eta \sqrt{5} |B_{3-3}^{III}|/(4W_0), \quad (21)$$

$$\psi_1 = \arg[B_{1-1}^{III}/\sqrt{2} + B_{3-1}^{III}\sqrt{3}], \quad (22)$$

$$\psi_3 = \arg[B_{3-3}^{III}]. \quad (23)$$

Equations (14) and (15) are similar to Eqs. (24) of [17] for the hydrogen atom, with the major difference being the $\beta_1^+ \sin \vartheta \cos(\varphi - \psi_1)$ term in (14). The origin of this difference may be understood from the following simplified discussion in the *LS* approximation: Two-photon ionization by a right-hand circularly polarized fundamental leads partly to a *p* wave, with the residual $2p^5 \ ^2P$ ion in the $M_f = 1$ state. Single-photon ionization, on the other hand, leads partly to an *s* wave, with the residual $2p^5 \ ^2P$ ion in the $M_f = 1$ state for a right-hand circularly polarized second harmonic and in the $M_f = -1$ state for the left-hand case. Interference of two pathways is only possible if final states are the same. While this interference of *s* and *p* waves is possible for co-rotating harmonics, it is forbidden for counter-rotating fields.

This was not the case for a residual ion in an *S* state, like atomic hydrogen [17] or alkali atoms. As in hydrogen, the co-rotating fields produce a single-lobe pattern, albeit in the C_s symmetry group with the symmetry plane perpendicular to the beam [see Fig. 2(b)] instead of C_{2h} for hydrogen, while the counter-rotating fields produce triple-lobe clover-leaf-like patterns [D_{3h} symmetry group with the principal axis along the beams, Fig. 2(c)]. The parametrization for the counter-rotating beams (15) is identical to the case of hydrogen (see Eqs. (24) of [17]). It will be seen below that the additional term β_1^+ , appearing for neon in (14), can noticeably suppress coherent control in some cases.

The symmetry of the PAD may be understood by looking carefully into the strength of the ionizing electric field, which is an effective way to analyze nonlinear processes [35,48,49]. The origin for the asymmetry in the process considered here is the following: When a field configuration appears, it repeats after every period. For co-rotating harmonics, the electric vectors coincide once in each period [Fig. 3(a)], while they coincide three times in each period for counter-rotating harmonics [Fig. 3(b)]. In a classical description, the electron would immediately follow the electric field vector. Quantum

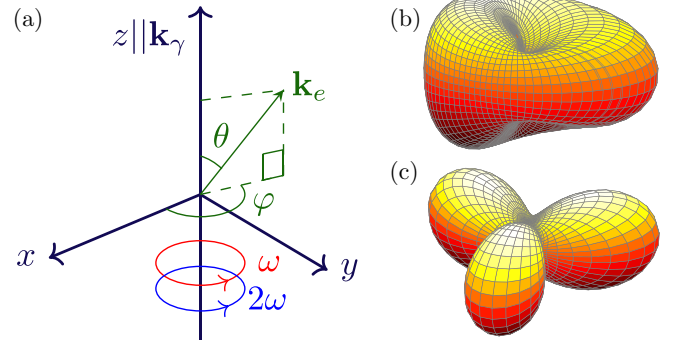


FIG. 2. The coordinate system (a) and typical PADs for co-rotating (b) and counter-rotating (c) fields. The calculation was performed in the PT model with $\omega = E_{3s'}$, $\eta = 0.1$, and $I = 10^{12}$ W/cm².

ionization, however, involves a scattering phase, and hence the resulting PAD in the plane containing the laser polarization rotates away from the field by the angle corresponding to the phase difference between the one- and two-photon ionization channels $\Delta_l^{(1)} - \Delta_l^{(2)}$ [17] (solid red lines in Fig. 3). When there are several ionization channels, the rotation angle differs for each set of matrix elements. For a multielectron atom ionized by co-rotating harmonics, these patterns with different rotation angles are summed. It follows from Eqs. (13)–(15) that the dominant effect of varying the relative phase between the harmonics is a rotation of the PAD around the direction of the beams. That would actually be the only effect within perturbation theory for long pulses (i.e., within PT and RWA). This can be understood because changing the relative phase of two circularly polarized long pulses rotates the direction along which the electric strengths of the harmonics coincide: e.g., for $\phi = 0$ they coincide along the *x* axis, for $\phi = \pi/2$ along the *y* axis. We set $\phi = 0$ below.

We employ three different computational models to describe the ionization of neon by a bichromatic field: Lowest-order time-dependent perturbation theory (PT) for a pulse of finite length; lowest-order perturbation theory for an infinitely long “pulse” (PT_∞), and direct numerical solution of the TDSE. These approaches were already presented in

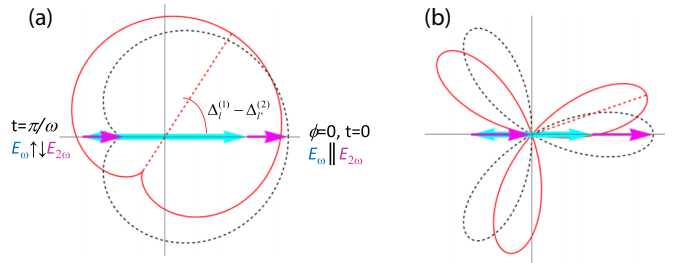


FIG. 3. Electric field strength (black dashed line) for co-rotating (a) and counter-rotating (b) harmonics with zero relative phase $\phi = 0$, and a modeled PAD (solid red line) in the plane perpendicular to the pulse beam with a difference in the scattering phases of $\Delta_l^{(1)} - \Delta_l^{(2)} = 1$. For co-rotating harmonics, the PAD rotates by 1 rad, while it rotates by $1/3$ rad in the counter-rotating case.

TABLE I. States in Racah notation and their spectroscopic designation \mathcal{N} for selected states, experimental excitation energies [56] (in eV), and leading eigenvector components.

State	\mathcal{N}	Energy	Leading terms in multiconfiguration expansion
$2p^6\ ^1S$		–	$93\% 2p^6\ ^1S\rangle + 6\% 2p^53p\ ^1S\rangle + 1\% 2p^43p^2\ ^1S\rangle^a$
$2p^5(^2P_{3/2})3s[3/2]_1$	$3s$	16.67	$10\% 2p^53s\ ^1P\rangle + 90\% 2p^53s\ ^3P\rangle$
$2p^5(^2P_{1/2})3s'[1/2]_1$	$3s'$	16.84	$90\% 2p^53s\ ^1P\rangle + 10\% 2p^53s\ ^3P\rangle$
$2p^5(^2P_{3/2})4s[3/2]_1$	$4s$	19.68	$48\% 2p^54s\ ^1P\rangle + 52\% 2p^54s\ ^3P\rangle$
$2p^5(^2P_{1/2})4s'[1/2]_1$	$4s'$	19.78	$52\% 2p^54s\ ^1P\rangle + 48\% 2p^54s\ ^3P\rangle$
$2p^5(^2P_{3/2})3d[1/2]_1$		20.03	$21\% 2p^53d\ ^1P\rangle + 77\% 2p^53d\ ^3P\rangle + 1\% 2p^53d\ ^3D\rangle$
$2p^5(^2P_{3/2})3d[3/2]_1$		20.04	$52\% 2p^53d\ ^1P\rangle + 10\% 2p^53d\ ^3P\rangle + 38\% 2p^53d\ ^3D\rangle$
$2p^5(^2P_{1/2})3d[3/2]_1$		20.14	$27\% 2p^53d\ ^1P\rangle + 12\% 2p^53d\ ^3P\rangle + 61\% 2p^53d\ ^3D\rangle$

^aSum of three terms with $2p^4\ ^3P$, 1D , 1S core states.

[19]. Since additional computational details can be found in [50–55], we only discuss the relevant modifications below.

The PT_∞ and TDSE models are both nonrelativistic and employ a single-active-electron approximation with the same potential describing the neon atom. In the PT model, we use multiconfiguration Hartree-Fock (MCHF) intermediate-coupling wave functions [57], which were further improved in comparison with [19]. Specifically, the $1s$, $2s$, $2p$ orbitals were obtained in a self-consistent calculation of the ionic $\text{Ne}^+(1s^22s^22p^5\ ^2P)$ ground state. These orbitals were then frozen, and the physical $3s$, $4s$, $3d$ orbitals were obtained in single-configuration $1s^22s^22p^5nl\ ^1P$ ($nl = 3s, 4s, 3d$) calculations. A $3\bar{p}$ correlation orbital was introduced to optimize the energy of the ground state on the mixed $2p^6 + 2p^53\bar{p} + 2p^43\bar{p}^2$ configurations. Finally, we mixed all configurations associated with single and double promotions of the $2p$ electron(s) by the above electronic states and applied the semirelativistic Breit-Pauli Hamiltonian to obtain the final configuration- and term-mixing coefficients. The above model improves the ionization potential and reproduces the angular anisotropy parameter β for single-photon ionization in good agreement with experiment [58].

The configuration mixing in the current model is stronger than that reported in our previous paper [19]. Table I shows some spectroscopic parameters of our PT model. The mixing coefficients strongly deviate from those of the pure LS - and jK -coupling schemes (not shown). We then used the experimental excitation thresholds in the calculations of the PADs. For the single-active-electron nonrelativistic PT_∞ and TDSE models, where the fine-structure splitting is neglected, we shifted the energies of the single-electron $3s$ and $4s$ states to match the calculated energy with the experimental energies averaged over the appropriate configurations.

III. RESULTS AND DISCUSSION

Figures 4(a) and 4(c) exhibit the angular anisotropy parameters as a function of the fundamental frequency. Within the second-order PT approach, $\beta_2^+ = \beta_2^-$, $\beta_3^+ = \beta_3^-$, and $\beta_1^- = 0$. The TDSE calculations show that $\beta_3^+ \approx \beta_3^-$ and $\beta_1^- \approx 0$, but $\beta_2^+ \neq \beta_2^-$ at a photon energy in resonance with the strong radiative transition between the ground state and the $3s'$ state. This difference is mainly due to transitions involving the

temporary recapture of an electron. For instance, ionization by the second harmonic could be followed by capture of an electron from the continuum state back to the $3s'$ state (this is only possible for co-rotating harmonics), and first-harmonic ionization could interfere with direct second-harmonic ionization. The asymmetry of this interference with the helicity of the second harmonic results in a difference between β_2^+ and β_2^- near a resonance. This effect cannot be described by second-order PT.

We confirmed the above interpretation of a strong-field effect by lowering the peak intensity by a factor of 2, i.e., setting $I = 5 \times 10^{11}$ W/cm². We found that the difference between β_2^+ and β_2^- was reduced by a factor of 3. The PT and TDSE results are in reasonable agreement with each other in the vicinity of the $3s$ state. The differences between the results obtained in the two approaches (except for the above-mentioned strong-field effect) are mostly due to the differences in the spectroscopic models. For example, the PT calculations exhibit weak features near the $3s$ state [Fig. 4(a)] due to the fine-structure splitting, which is not accounted for in the single-active electron TDSE calculations. Similarly, the shapes of the PT and TDSE curves are different in the vicinity of the $4s$ states [Fig. 4(c)], although the maximum values of the anisotropy parameters agree. This difference is also a manifestation of the fine-structure splitting in the PT model. Although not resolved for the chosen pulse duration of $N = 250$ optical cycles (50–65 fs), accounting for the fine-structure splitting shifts the position of the zeros.

The energy dependence of the angle ψ_k is determined by an interplay between two-photon ionization into p and f waves. The former is dominated by resonant ionization via the $3s$ and $4s$ states, while the latter is dominated by nonresonant ionization through infinite sets of virtual nd and ϵd states or, in other words, the potential part of the ionization amplitude. As a result, the phase of the p -wave amplitude changes by π when the photon energy crosses the resonance. The longer the pulse, the sharper is the phase jump. These π jumps are seen in both angles ψ_1 and ψ_3 , in the vicinity of the $3s'$ state [see Fig. 4(b)], while an additional π jump in ψ_1 and ψ_3 (out of range of the figure) is due to a vanishing $|\beta_k|$. For an infinitely long pulse, the same features would be observed in the vicinity of the $4s$ and $4s'$ states (see Figs. 3(c) and 3(d) of [19]). The main contribution to both β_1^+ and β_3^\pm comes

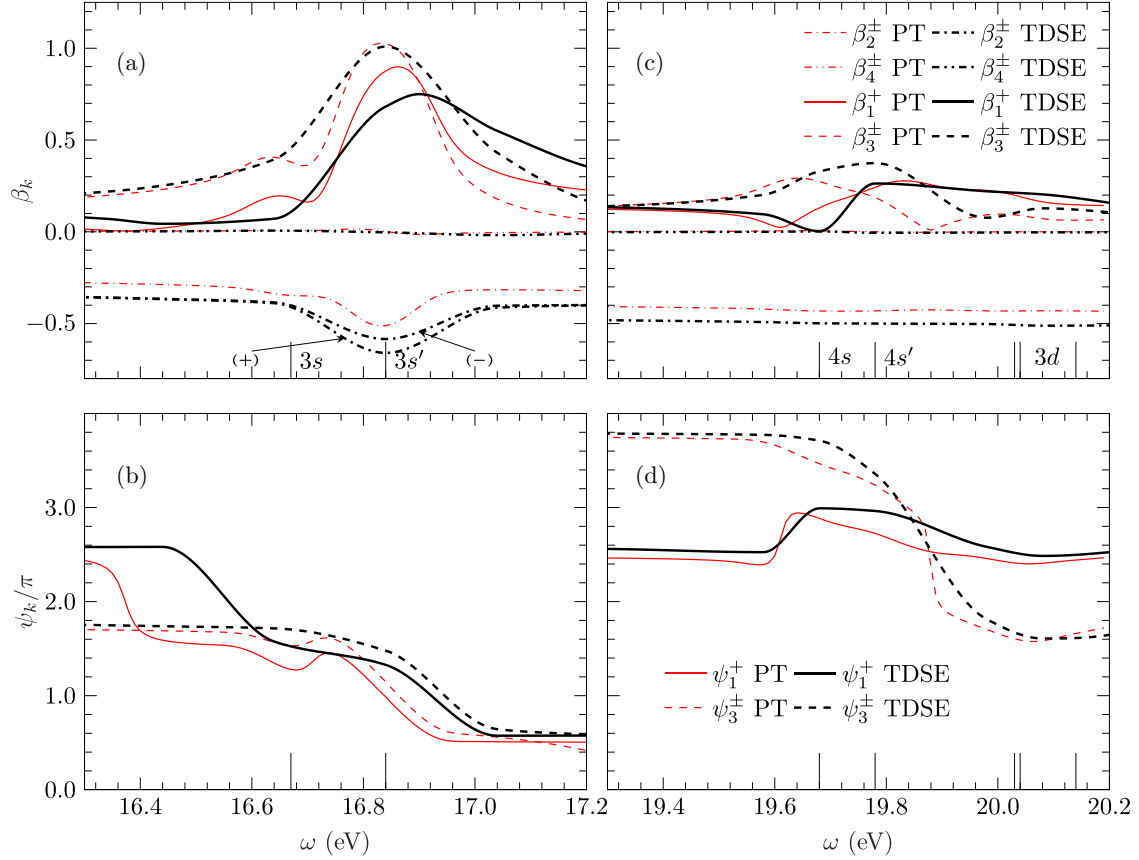


FIG. 4. Angular anisotropy parameters β_k ($k = 1, 2, 3, 4$) and the angles ψ_k ($k = 1, 3$). Black thick lines: TDSE, red thin lines: PT. Left panels: The region near the $3s$ states, right panels: The region near the $4s$ and $3d$ states. The pulse parameters are: $I = 10^{12}$ W/cm², $\eta = 0.1$, $N = 250$. Those parameters that exist in both the co-rotating and counter-rotating cases coincide in the PT approach. The only visible difference in the TDSE results is observed for β_2^+ and β_2^- in (a).

from interference between two-photon ionization into the f wave and one-photon ionization into the d wave. Furthermore, assuming no significant contributions from other channels, $\beta_1^+ = \beta_3^+$ and $\psi_1 = \psi_3 + \pi$.

Since it is difficult to extract the angular anisotropy parameters directly from the experimental data, it is often more practical to introduce the maximum polar asymmetry of the PAD, as in the case of hydrogen [17]. This polar asymmetry is defined as

$$A^v(\vartheta, \varphi) = \frac{W^v(\vartheta, \varphi) - W^v(\vartheta, \varphi + \pi)}{W^v(\vartheta, \varphi) + W^v(\vartheta, \varphi + \pi)}, \quad (24)$$

where $W^v(\vartheta, \varphi) \equiv dW^v/d\Omega$ and $v = (-)$ or $v = (+)$. The asymmetry (24) vanishes for incoherent one- and two-photon ionization, when the PAD becomes axially symmetric. For the counter-rotating fields, $v = (-)$, Eq. (15) shows that the maximum asymmetry A_{\max}^- is observed at $\vartheta = \pi/2$, $3\varphi = \psi_3$.

For the co-rotating fields, $v = (+)$, the answer is not so straightforward. For practical convenience, therefore, we consider the maximum asymmetry in the plane perpendicular to the beam ($\vartheta = \pi/2$). The dependence of (24) on φ is then seen from Eqs. (14), (15), and

$$A_{\max}^v = |A^v(\pi/2, 0) + iA^v(\pi/2, \pi/2)|, \quad (25)$$

while the corresponding polar angle of the maximum signal is observed at

$$\varphi_{\max}^v = \arg[A^v(\pi/2, 0) + iA^v(\pi/2, \pi/2)]. \quad (26)$$

In Eqs. (25) and (26) one can take any other pair of conjugated angles $\{\varphi, \varphi + \pi/2\}$ instead of $\{0, \pi/2\}$.

The asymmetries (24) and (25), as well as the angle (26), may be considered as controlled parameters, together with β_k^v and ψ_k^v . At the same time, for the incoherent process, only β_2^v and β_4^v do not vanish.

In Fig. 5 the polar asymmetries (24) are displayed for co- and counter-rotating fields calculated within our three models for $\vartheta = \pi/2$, two angles $\varphi = 0$, $\varphi = \pi/2$, and the relative phase between the harmonics $\phi = 0$. The polar diagrams exhibit the maximum asymmetries (25) and the corresponding observation angle (26) as they vary with the fundamental frequency. These variations are sharp near the resonances, while A_{\max} and φ_{\max} remain almost constant between the resonances.

The TDSE calculations show that the anisotropy parameters of high rank are small. Specifically, $\beta_{k>4} < 0.005$ suggests the validity of the parametrization (2,14,15) for the intensity discussed here. From previous calculations for linearly polarized harmonics, we also know that the parametrization is valid up to $I \approx 5 \times 10^{13}$ W/cm². Additional channels

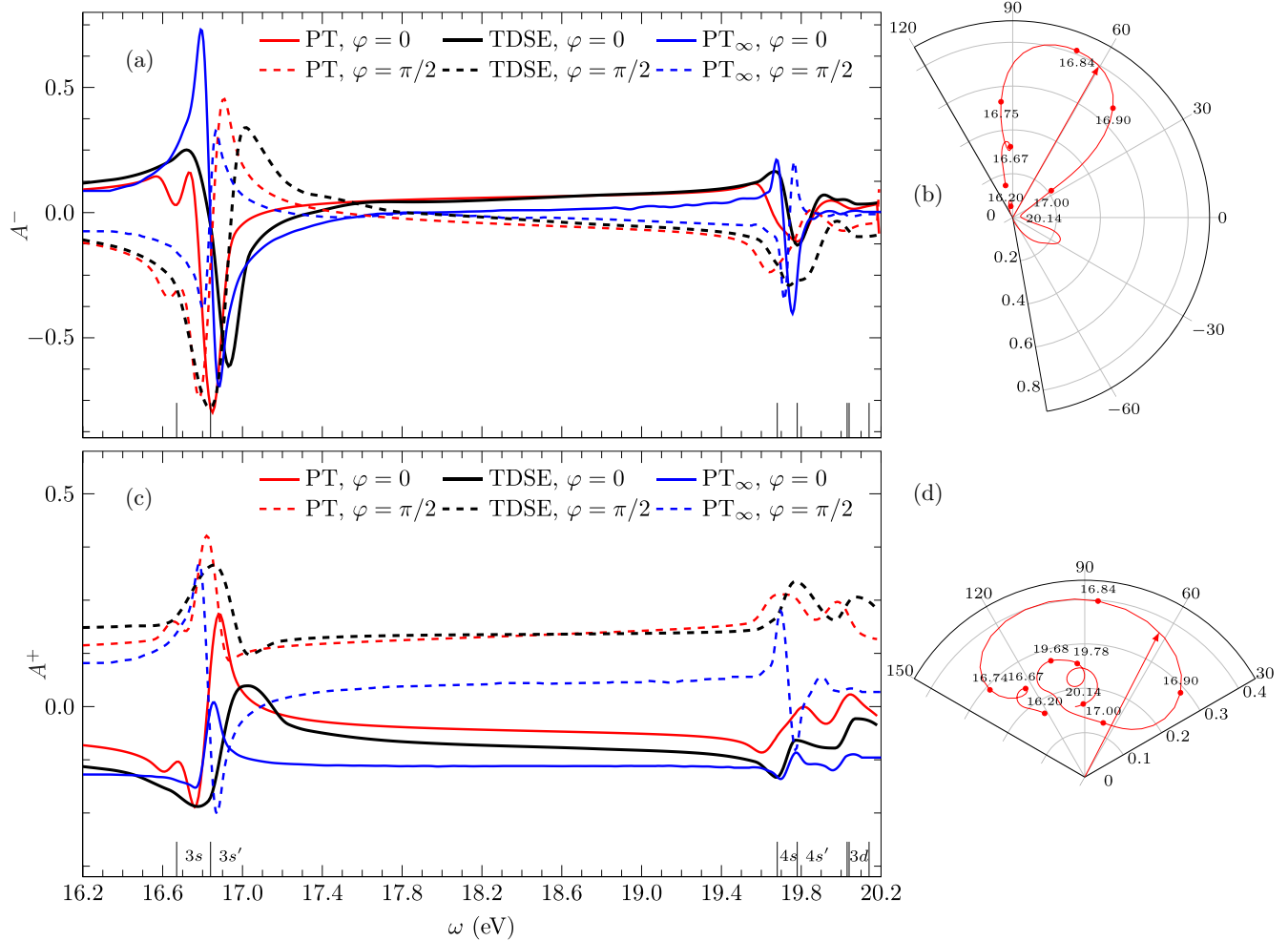


FIG. 5. Polar asymmetries A^- (a) and A^+ (c) for the phase $\phi = 0$ between the fundamental and its second harmonic for two angles $\varphi = 0, \pi/2$ [$\vartheta = \pi/2$, see Eq. (25)]. (b) and (d): The amplitudes of maximum polar asymmetry and polar angle φ for its observation, as obtained with the PT model. The number along the curves marked corresponds to the photon energy. The upper panels are for opposite helicities, the bottom ones for equal helicities. The pulse parameters are the same as in Fig. 4.

do not play an important role, even though saturation at resonance is achieved earlier at $I \approx 10^{13}$ W/cm 2 (Fig. 6 of [19]).

An essential difference between the current results for neon and those for hydrogen [17] is that for hydrogen A_{\max} and φ_{\max} were the same for co- and counter-rotating fields. In neon the patterns are different. This difference originates from the interplay between many ionization channels. For a strong resonance, such as $2p^53s$, the maximum asymmetry for counter-rotating fields is much larger than for co-rotating fields. With a weakening of the resonance ionization pathway, leading to the domination of the direct two-photon ionization into the f wave, the asymmetries become comparable and even larger than for co-rotating fields. The d and f channels dominate in the nonresonant region, and it follows from (5), (8), and (24) that $A^+(\vartheta, \varphi) = -2A^-(\vartheta, \varphi)$. Both time-dependent models (TDSE and PT) tend to show the extremum of the asymmetry near the resonances, while PT $_{\infty}$ predicts zero asymmetry at the resonance and two pronounced extrema on both sides [the indication to this splitting could be seen in PT and TDSE for longer pulses, see Figs. 6(a) and 6(b) region of small η]. In contrast to hydrogen [17] and neon with linearly polarized

fields [18,19], A_{\max}^v cannot reach unity at the extrema with circularly polarized light, despite the fact that A_{\max}^- can get close to 1.0 if a resonance is strong enough [cf. Fig. 5(a)]. For A_{\max}^+ , the value at the extrema depends on the interplay between the s and d channels and is always less than unity.

Figure 6 provides a general view of the evolution of the maximum asymmetry with varying the relative harmonic strength η . To maximize the asymmetry generated by the interference between the one-photon and two-photon ionization channels they should be comparable in strength. The one-photon ionization channels do not contain resonances, and hence the corresponding amplitudes vary smoothly in the region of interest. In contrast, the two-photon channels include resonances, predominantly in the p -wave channel, due to the intermediate ns discrete states, in addition to the smooth two-photon transitions into the f -wave channels. Figures 6(a) and 6(b) demonstrate that the influence of the resonances is more important for the counter-rotating fields. For harmonic ratios of $\eta \approx 0.3$ (for $3s$) and $\eta \approx 0.02$ (for $4s$), the maximum polar asymmetry A_{\max}^- approaches unity. A_{\max}^- is decreasing for both higher and lower values of η , respectively, due to

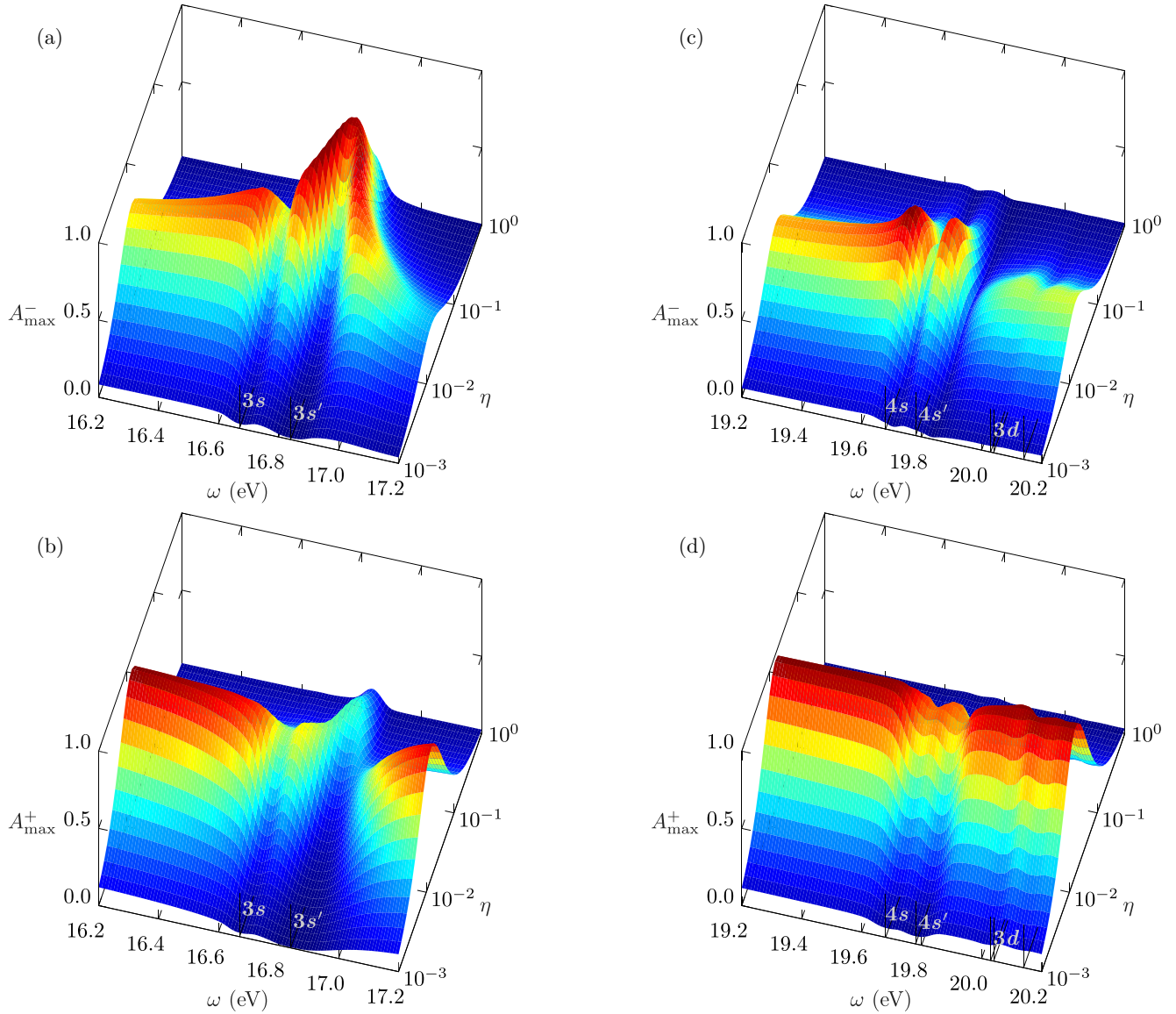


FIG. 6. Maximum polar asymmetry as a function of the fundamental frequency ω and harmonic strength ratio η for counter-rotating (upper panels) and co-rotating (lower panels) harmonic fields. The left panels present the region near the $3s$ state, the right panels present the region near the $4s$ and $3d$ states. The results are from PT calculations with $I = 10^{12}$ W/cm² and $N = 500$.

the domination of either the one-photon or the two-photon ionization channels, thereby leading to a small interference term in the PAD. Away from the resonance, a large polar asymmetry is reached at smaller relative intensity of the second harmonic $\eta < 0.02$, but it remains below the asymmetry values at the resonance. For the co-rotating fields, the asymmetry approaches unity away from the resonance region at small $\eta < 0.1$, showing the dominant role of the nonresonant amplitudes, and then drops down near the resonances.

Finally, Eq. (14) shows that there are six parameters that describe the PAD for co-rotating fields and four ionization channels. Consequently, three ratios of complex amplitudes determine the combined one- and two-photon ionization dynamics. This means that measurements of the PAD for the co-rotating fields are sufficient to extract all the magnitude ratios and the relative phases (up to modulo π) between the amplitudes. Except for an overall normalization factor, this makes it

possible to perform, within the limits of nonrelativistic lowest-order perturbation theory and the dipole approximation, a so-called complete photoionization experiment [30].

IV. OTHER PRACTICAL EXAMPLES

The ionization with two circularly polarized fields considered here and in [19] with two linearly polarized fields along the same direction are two special cases when it comes to breaking symmetry. If there is no coherence between the harmonics, then the PADs possess symmetry axes and, perpendicular to them, a symmetry plane. One of these symmetries is broken when coherent control is realized. From this point of view it is hardly practical to consider intermediate cases, such as elliptical polarization(s) or arbitrary angle between harmonic propagation directions, because most of them do not possess axial symmetry even for incoherent harmonics. The

criteria for realization of coherent control, therefore, would be ambiguous.

There is only one exception, namely when one harmonic is circularly polarized and the other one is linearly polarized along the propagation direction of the first one. Specifically, the field for a linearly polarized fundamental and a circularly polarized second harmonic (*LC*) can be cast as

$$\mathcal{E}^{LC}(t) = F(t)\{\mathbf{z} \cos \omega t + \eta[\mathbf{x} \cos(2\omega t + \phi) + \lambda \mathbf{y} \sin(2\omega t + \phi)]\}. \quad (27)$$

On the other hand, a circularly polarized fundamental and a linearly polarized second (*CL*) is written as

$$\mathcal{E}^{CL}(t) = F(t)[\mathbf{x} \cos \omega t + \mathbf{y} \sin \omega t + \eta \mathbf{z} \cos(2\omega t + \phi)]. \quad (28)$$

Since the intensity of a harmonic depends on its polarization, a meaningful comparison requires that η should be $\sqrt{2}$ times smaller than for circularly polarized harmonics in the first case and $\sqrt{2}$ times larger in the second case.

In the first case the PAD takes the same form as (14) for equal helicities:

$$\begin{aligned} \frac{dW^{LC}}{d\Omega} = \frac{W_0}{4\pi} & \left[1 + \beta_2^{LC} P_2(\cos \vartheta) + \beta_4^{LC} P_4(\cos \vartheta) \right. \\ & + \beta_1^{LC} \sin \vartheta \cos(\varphi - \psi_1^{LC}) \\ & \left. - \beta_3^{LC} \sin^3 \vartheta \cos(\varphi - \psi_3^{LC}) \right]. \quad (29) \end{aligned}$$

It possesses a single-lobe pattern (symmetry group is C_s), but the parameters in Eqs. (29) and (14) are not related, because two-photon ionization by linearly polarized radiation allows channel(s) with total angular momentum $J = 0$, which are forbidden for circular polarization. The equations for β_k^{LC} via the parameters B^{LC} remain the same as given in (16)–(20) and (22) for equal helicities. The representation of the angular anisotropy parameters in terms of amplitudes is given in the Appendix. A typical PAD is shown in Fig. 7(a). There is no interference contribution along the z axis, i.e., the polarization direction of the fundamental. A more pronounced interference pattern appears in the xy plane.

The PAD for a circularly polarized fundamental and a linearly polarized second harmonic is parametrized as

$$\begin{aligned} \frac{dW^{CL}}{d\Omega} = \frac{W_0}{4\pi} & \left[1 + \beta_2^{CL} P_2(\cos \vartheta) + \beta_4^{CL} P_4(\cos \vartheta) \right. \\ & \left. + \beta_3^{CL} \cos \vartheta \sin^2 \vartheta \cos(2\varphi - \psi_3^{CL}) \right]. \quad (30) \end{aligned}$$

This case is related to (6)–(8) for the opposite helicities via the transformations $B_k^{II(CL)} \equiv B_k^{II}$, $B_0^{I(CL)} = B_0^I$, $B_2^{I(CL)} = -2B_2^I$, and $B_{3-2}^{III(CL)} = B_{3-3}/\sqrt{3}$ (provided that the strength F_0 of the linearly polarized harmonic is $\sqrt{2}$ higher than for the circularly polarized case). Equations (16)–(18) remain the same, while (21) and (23) are modified as follows:

$$\beta_3^{CL} = \eta \sqrt{30} |B_{3-2}^{III(CL)}| / (4W_0), \quad (31)$$

$$\psi_3^{CL} = \arg[B_{3-2}^{III(CL)}]. \quad (32)$$

Hence $\beta_3^{CL} = \sqrt{2}\beta_3^-$ (provided that $\eta^{CL} = \sqrt{2}\eta^-$) and $\psi_3^{CL} = \psi_3$. The symmetry group is S_2 and example of typical PAD is

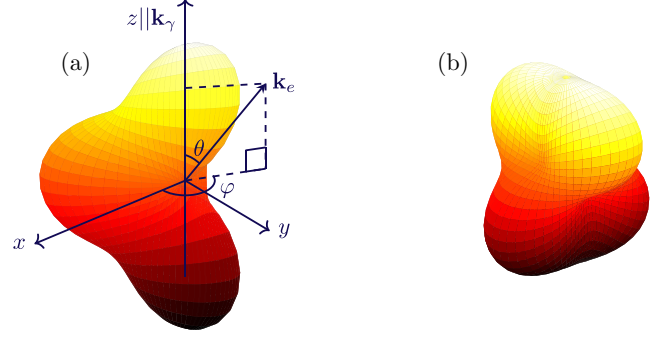


FIG. 7. Typical PADs for a linearly polarized fundamental and right-hand circularly polarized second harmonic for $\eta = 0.1/\sqrt{2}$ (a) and vice versa at $\eta = 0.1\sqrt{2}$ (b). The calculation was performed in the PT model with $\omega = E_{3s'}$, $I = 10^{12}$ W/cm².

shown in Fig. 7(b). From the parametrization (30) one can see that interference contributes most at the magic angle $\vartheta_{\text{mag}} = \arccos[1/\sqrt{3}]$, producing two horns for $\varphi = \psi_3^{CL}/2$ and $\varphi = \psi_3^{CL}/2 + \pi$. The same happens in the lower hemisphere at $\vartheta = \pi - \arccos[1/\sqrt{3}]$ and $\varphi = \psi_3^{CL}/2 \pm \pi/2$. This setup may be especially attractive for practical purposes, because at the magic angle there are only minor contributions from incoherent terms to the PAD due to $P_2(\cos \vartheta_{\text{mag}}) = 0$.

In both cases *CL* and *LC*, varying the phase between the harmonics rotates the PAD around the z axis. The efficiency of control, i.e., the asymmetry, only depends on the harmonic strengths ratio η .

V. SUMMARY AND CONCLUSIONS

We have investigated the coherent control of the photoelectron angular distribution from the valence $2p$ shell of atomic neon after circularly polarized bichromatic ionization by a fundamental frequency and its second harmonic in the vicinity of intermediate resonances. The maximum asymmetry of the PAD in the plane normal to the photon beams (the “polar asymmetry”) and the corresponding rotation angle of the symmetry axis in this plane are the main parameters to control, while the relative intensities, the helicities, the relative phases of the two circularly polarized fields, the fundamental frequency, and the time duration of the pulses represent the controlling parameters. While varying the relative phase of the harmonics for collinearly polarized fields provides control of the PAD asymmetry, it only causes a rotation of the PAD around the beam direction for circularly polarized beams.

For neon and, by similar considerations, for ionization of the valence p subshells of other heavy noble gases, the PADs for co- and counter-rotating fields differ by one term, in contrast to ionization of s electrons from atomic hydrogen or the alkali atoms, where the parametrizations are identical. Thus, in noble gases other than helium, the behavior of the polar asymmetry is more intricate. For counter-rotating fields, the polar asymmetry is larger and originates from intermediate resonances in the two-photon ionization pathway. For co-rotating fields, the influence of the intermediate resonances is weaker, and a polar asymmetry is already caused by the nonresonant ionization pathways.

In addition, we considered situations when one harmonic is circularly polarized and the other one is linearly polarized along the propagation direction of the first. For incoherent harmonics, ionization with such a field produces an axially symmetric PAD, and coherent control appears as a violation of that symmetry. The PAD pattern crucially depends on whether the first or the second harmonic is linearly polarized, with the second case appearing more promising from an experimental point of view.

Remarkably, for all cases considered in this work, there is a significant difference for right-hand and left-hand polarized harmonic(s). The realization of coherent control manifests itself as a differential circular dichroism. Furthermore, experiments on coherent control with circularly polarized harmonics might open a way to perform complete photoionization experiments through the process of joint one-photon and two-photon ionization. We hope that the present study will

motivate experimentalists and other theoretical groups to also investigate this interesting problem.

ACKNOWLEDGMENTS

The authors benefited greatly from stimulating discussions with Giuseppe Sansone, Kevin Prince, and Kiyoshi Ueda. E.V.G., M.M.P and E.I.S. acknowledge support from the Foundation for the Advancement of Theoretical Physics and Mathematics BASIS via the Junior Leader program. The work of N.D. and K.B. was supported by the United States National Science Foundation under Grants No. PHY-1430245 and No. PHY-1803844, as well as the XSEDE allocation PHY-090031. The TDSE calculations were performed on Stampede2 at the Texas Advanced Computing Center and SuperMIC at the Center for Computation & Technology at Louisiana State University.

APPENDIX

Below we present the parameters B^{CL} and B^{LC} for one linearly and the other circularly polarized harmonics in terms of reduced ionization amplitudes. Note that $B^{I(LC)} \equiv B^I$ [Eq. (6)] and $B^{II(CL)} \equiv B^{II}$ [Eq. (7)]:

$$B_k^{I(CL)} = (-1)^{L_f} \sum_{l'l'} \hat{l}'(10, 10 | k0)(l0, l'0 | k0) \begin{Bmatrix} 1 & 1 & k \\ l' & l & L_f \end{Bmatrix} \exp[i(\Delta_l^{(1)} - \Delta_{l'}^{(1)})] |T_\lambda^{(1)}|^2 D_{0 \rightarrow L_f l, 1}^{(0)} D_{0 \rightarrow L_f l', 1}^{(0)*}, \quad (\text{A1})$$

$$B_k^{II(LC)} = (-1)^{L_f} \sum_{\substack{l'l' \\ LL'S}} (-1)^{S+L+L'} \hat{l}' \hat{j} \hat{j}'(l0, l'0 | k0)(J0, J0 | k0)(10, 10 | J0)(10, 10 | J'0) \exp[i(\Delta_l^{(2)} - \Delta_{l'}^{(2)})] \\ \times \hat{L} \hat{L}' \begin{Bmatrix} L & L' & k \\ l' & l & L_f \end{Bmatrix} \begin{Bmatrix} L & L' & k \\ J' & J & S \end{Bmatrix} \left(\sum_{nL_n} \alpha_{10}^{\zeta_n*} \alpha_{L_n S}^{\zeta_n} T_{E_n}^{(2)} \begin{Bmatrix} S & L & 2 \\ 1 & 1 & L_n \end{Bmatrix} D_{0 \rightarrow n, 1}^{(0)} D_{n, L_n \rightarrow L_f l, L}^{(S)} \right) \\ \times \left(\sum_{n'L_n} \alpha_{10}^{\zeta_{n'}} \alpha_{L_n' S}^{\zeta_{n'}*} T_{E_{n'}}^{(2)*} \begin{Bmatrix} S & L' & 2 \\ 1 & 1 & L_n' \end{Bmatrix} D_{0 \rightarrow n', 1}^{(0)*} D_{n', L_n' \rightarrow L_f l', L'}^{(S)*} \right), \quad (\text{A2})$$

$$B_{k-2}^{III(CL)} = \frac{(-1)^{L_f}}{\sqrt{3}} \sum_{l'l'} \hat{l}'(l0, l'0 | k0)(10, 2-2 | k-2) \exp[i(\Delta_l^{(1)} - \Delta_{l'}^{(2)})] \\ \times \begin{Bmatrix} 2 & 1 & k \\ l & l' & L_f \end{Bmatrix} T_\lambda^{(1)} D_{0 \rightarrow L_f l, 1}^{(0)} \left(\sum_{n'L_n} |\alpha_{10}^{\zeta_{n'}}|^2 T_{E_{n'}}^{(2)*} D_{0 \rightarrow n', 1}^{(0)*} D_{n', L_n' \rightarrow L_f l', 2}^{(0)*} \right), \quad (\text{A3})$$

$$B_{k-1}^{III(LC)} = \frac{(-1)^{L_f}}{\sqrt{3}} \sum_{l'l'} \hat{l}'(l0, l'0 | k0)(1-1, L'0 | k-1)(10, 10 | L'0) \exp[i(\Delta_l^{(1)} - \Delta_{l'}^{(2)})] \\ \times \begin{Bmatrix} L' & 1 & k \\ l & l' & L_f \end{Bmatrix} T_\lambda^{(1)} D_{0 \rightarrow L_f l, 1}^{(0)} \left(\sum_{n'L_n} |\alpha_{10}^{\zeta_{n'}}|^2 T_{E_{n'}}^{(2)*} D_{0 \rightarrow n', 1}^{(0)*} D_{n', L_n' \rightarrow L_f l', L'}^{(0)*} \right). \quad (\text{A4})$$

Note that the $T^{(1)}$ and $T_{E_n}^{(2)}$ factors for circularly polarized harmonics defined in (11) and (12) are larger by factors of $\sqrt{2}$ and 2, respectively, than for the linearly polarized case defined in Eqs. (9) and (10) of [16]. In (A3) only channels with $L = J = 2$ are allowed, while in (A4) both $L = J = 0, 2$ for the two-photon amplitudes are possible. In order to cast the parametrization (29) into the same form as (14), we choose the second harmonic to be left-hand circularly polarized [see Eq. (A4)]. For right-hand circular polarization one should make the replacement $\varphi \rightarrow -\varphi$.

[1] M. Shapiro and P. Brumer, *J. Chem. Phys.* **84**, 4103 (1986).

[2] M. Shapiro and P. Brumer, in *Advances in Atomic, Molecular, and Optical Physics*, edited by B. Bederson and H. Walther (Academic, San Diego, 2000), Vol. 42, p. 287.

[3] F. Ehloltzky, *Phys. Rep.* **345**, 175 (2001).

[4] P. Brumer and M. Shapiro, *Principles of the Quantum Control of Molecular Processes* (Wiley-VCH, Berlin, 2003).

[5] M. Shapiro and P. Brumer, *Phys. Rep.* **425**, 195 (2006).

- [6] V. A. Astapenko, *Quantum Electron.* **36**, 1131 (2006).
- [7] C. Brif, R. Chakrabati, and H. Rabitz, *New J. Phys.* **12**, 075008 (2010).
- [8] A. H. Zewail, *J. Phys. Chem. A* **104**, 5660 (2000).
- [9] L. A. A. Nikolopoulos, E. P. Benis, P. Tzallas, D. Charalambidis, K. Witte, and G. D. Tsakiris, *Phys. Rev. Lett.* **94**, 113905 (2005).
- [10] Y. Nabekawa, T. Shimizu, T. Okino, K. Furusawa, H. Hasegawa, K. Yamanouchi, and K. Midorikawa, *Phys. Rev. Lett.* **97**, 153904 (2006).
- [11] A. H. Zewail, *Science* **328**, 187 (2010).
- [12] O.-H. Kwon and A. H. Zewail, *Science* **328**, 1668 (2010).
- [13] K. C. Prince, E. Allaria, C. Callegari, R. Cucini, G. D. Ninno, S. D. Mitri, B. Diviacco, E. Ferrari, P. Finetti, D. Gauthier *et al.*, *Nat. Photon.* **10**, 176 (2016).
- [14] L. Giannessi, E. Allaria, K. C. Prince, C. Callegari, G. Sansone, K. Ueda, T. Morishita, C. N. Liu, A. N. Grum-Grzhimailo, E. V. Gryzlova *et al.*, *Sci. Rep.* **8**, 7774 (2018).
- [15] M. D. Fraia, O. Plekan, C. Callegari, K. C. Prince, L. Giannessi, E. Allaria, L. Badano, G. De Ninno, M. Trovò, B. Diviacco *et al.*, *Phys. Rev. Lett.* **123**, 213904 (2019).
- [16] A. N. Grum-Grzhimailo, E. V. Gryzlova, E. I. Staroselskaya, J. Venzke, and K. Bartschat, *Phys. Rev. A* **91**, 063418 (2015); **93**, 019901(E) (2016).
- [17] N. Douguet, A. N. Grum-Grzhimailo, E. V. Gryzlova, E. I. Staroselskaya, J. Venzke, and K. Bartschat, *Phys. Rev. A* **93**, 033402 (2016).
- [18] N. Douguet, E. V. Gryzlova, E. I. Staroselskaya, K. Bartschat, and A. N. Grum-Grzhimailo, *Eur. Phys. J. D* **71**, 105 (2017).
- [19] E. V. Gryzlova, A. N. Grum-Grzhimailo, E. I. Staroselskaya, N. Douguet, and K. Bartschat, *Phys. Rev. A* **97**, 013420 (2018).
- [20] U. Heinzmann, *Phys. Scr.* **T17**, 77 (1987).
- [21] U. Fano, *Phys. Rev.* **178**, 131 (1969).
- [22] M. Dörr, R. M. Potvliege, D. Proulx, and R. Shakeshaft, *Phys. Rev. A* **43**, 3729 (1991).
- [23] M. Pont and M. Gavrilá, *Phys. Rev. Lett.* **65**, 2362 (1990).
- [24] P. Dietrich, N. H. Burnett, M. Ivanov, and P. B. Corkum, *Phys. Rev. A* **50**, R3585(R) (1994).
- [25] F. A. Weihe, S. K. Dutta, G. Korn, D. Du, P. H. Bucksbaum, and P. L. Shkolnikov, *Phys. Rev. A* **51**, R3433(R) (1995).
- [26] A. Fleischer, O. Kfir, T. Diskin, P. Sidorenko, and O. Cohen, *Nat. Photon.* **8**, 543 (2014).
- [27] P.-C. Huang, C. Hernández-García, J.-T. Huang, P.-Y. Huang, C.-H. Lu, L. Rego, D. D. Hickstein, J. L. Ellis, A. Jaron-Becker, A. Becker *et al.*, *Nat. Photon.* **12**, 349 (2018).
- [28] P. F. Liao and G. C. Bjorklund, *Phys. Rev. A* **15**, 2009 (1977).
- [29] N. L. Manakov, M. V. Frolov, B. Borca, and A. F. Starace, *J. Phys. B* **36**, R49 (2003).
- [30] H. Kleinpoppen, B. Lohmann, and A. N. Grum-Grzhimailo, *Perfect/Complete Scattering Experiments* (Springer, Berlin Heidelberg, 2013).
- [31] S. Fukahori, T. Ando, S. Miura, R. Kanya, K. Yamanouchi, T. Rathje, and G. G. Paulus, *Phys. Rev. A* **95**, 053410 (2017).
- [32] T. Mazza, M. Ilchen, A. Rafipoor, C. Callegari, P. Finetti, O. Plekan, K. Prince, R. Richter, M. Danailov, A. Demidovich *et al.*, *Nat. Commun.* **5**, 3648 (2014).
- [33] N. I. Shvetsov-Shilovski, S. P. Goreslavski, S. V. Popruzhenko, and W. Becker, *Phys. Rev. A* **77**, 063405 (2008).
- [34] Christian Per Juul Martiny and L. B. Madsen, *Phys. Rev. Lett.* **97**, 093001 (2006).
- [35] S. Eckart, M. Kunitski, I. Ivanov, M. Richter, K. Fehre, A. Hartung, J. Rist, K. Henrichs, D. Trabert, N. Schlott *et al.*, *Phys. Rev. A* **97**, 041402(R) (2018).
- [36] K. Lin, X. Gong, Q. Song, Q. Ji, W. Zhang, J. Ma, P. Lu, H. Pan, J. Ding, H. Zeng *et al.*, *J. Phys. B: At. Mol. Opt. Phys.* **49**, 025603 (2016).
- [37] H. R. Reiss, *Phys. Rev. A* **82**, 023418 (2010).
- [38] E. A. Pronin, A. F. Starace, M. V. Frolov, and N. L. Manakov, *Phys. Rev. A* **80**, 063403 (2009).
- [39] J. M. NgokoDjiokap, S. X. Hu, L. B. Madsen, N. L. Manakov, A. V. Meremianin, and A. F. Starace, *Phys. Rev. Lett.* **115**, 113004 (2015).
- [40] N. B. Baranova, B. Y. Zel'dovich, A. N. Chudinov, and A. A. Shul'ginov, *Zh. Eksp. Teor. Fiz.* **98**, 1857 (1990) [*Sov. Phys. JETP* **71**, 1043 (1990)].
- [41] Y.-Y. Yin, C. Chen, D. S. Elliott, and A. V. Smith, *Phys. Rev. Lett.* **69**, 2353 (1992).
- [42] H. Eichmann, A. Egbert, S. Nolte, C. Momma, B. Wellegehausen, W. Becker, S. Long, and J. K. McIver, *Phys. Rev. A* **51**, R3414 (1995).
- [43] N. L. Manakov, V. D. Ovsiannikov, and A. F. Starace, *Phys. Rev. Lett.* **82**, 4791 (1999).
- [44] A. Bolvinos, S. Cohen, and I. Lontos, *Phys. Rev. A* **77**, 023413 (2008).
- [45] R. E. Goetz, C. P. Koch, and L. Greenman, *Phys. Rev. Lett.* **122**, 013204 (2019).
- [46] V. B. Berestetskii, E. M. Lifshitz, and L. P. Pitaevskii, *Quantum Electrodynamics* (Butterworth-Heinemann, Oxford, 1982), Vol. 4.
- [47] D. A. Varshalovich, A. N. Moskalev, and V. K. Khersonskii, *Quantum Theory of Angular Momentum* (World Scientific, Singapore, 1988).
- [48] S. Eckart, M. Richter, M. Kunitski, A. Hartung, J. Rist, K. Henrichs, N. Schlott *et al.*, *Phys. Rev. Lett.* **117**, 133202 (2016).
- [49] L. Barreau, K. Veyrinas, V. Gruson, S. J. Weber, T. Auguste, J.-F. Hergott, F. Lepetit, B. Carré, J.-C. Houver, D. Dowek *et al.*, *Nat. Commun.* **9**, 4727 (2018).
- [50] A. N. Grum-Grzhimailo, B. Abeln, K. Bartschat, D. Weflen, and T. Urness, *Phys. Rev. A* **81**, 043408 (2010).
- [51] A. N. Grum-Grzhimailo, M. N. Khaerdinov, and K. Bartschat, *Phys. Rev. A* **88**, 055401 (2013).
- [52] I. A. Ivanov, A. S. Kheifets, K. Bartschat, J. Emmons, S. M. Buczek, E. V. Gryzlova, and A. N. Grum-Grzhimailo, *Phys. Rev. A* **90**, 043401 (2014).
- [53] A. E. Orel and T. N. Rescigno, *Chem. Phys. Lett.* **146**, 434 (1988).
- [54] B. Gao and A. F. Starace, *Phys. Rev. A* **39**, 4550 (1989).
- [55] E. I. Staroselskaya and A. N. Grum-Grzhimailo, *Vest. Mosk. Univ. Fiz.* **N5**, 45 (2015) [*Moscow Univ. Phys. Bull.* **70**, 374 (2015)].
- [56] NIST atomic spectra database, https://physics.nist.gov/PhysRefData/ASD/levels_form.html.
- [57] C. F. Fischer, T. Brage, and P. Johansson, *Computational Atomic Structure: An MCHF Approach* (IOP, Bristol, 1997).
- [58] B. Langer, in *Studies of Vacuum Ultraviolet and X-ray Processes*, edited by U. Becker (ANS, New York, 1992).